AIAA JOURNAL
Vol. 50, No. 12, December 2012

Tomographic Particle Image Velocimetry Measurements in a Bluff-Body Wake Flow

C. Christian Wolf* and Ralf Hörnschemeyer†
Institute of Aeronautics and Astronautics, 52062 Aachen, Germany

DOI: 10.2514/1.J051764

The wake flow of a bluff-based cylindrical body, representing a generic model of a rocket configuration, is investigated experimentally for subsonic inflow conditions. This study concentrates on turbulent structures in the shear layer between recirculation bubble and external flow. Tomographic particle image velocimetry was applied to determine the instantaneous velocity distribution of three-dimensional measurement volumes. The results are compared to standard planar particle image velocimetry measurements considering mean velocity and turbulence levels. The availability of volumetric data enables the application of vortex identification schemes based on the velocity gradient tensor $\nabla \boldsymbol{v}$, in this case Q- and λ_{Ci}-criterion. The selection of an appropriate onset threshold to separate vortical structures from measurement noise is discussed. A statistical analysis was carried out for different regions of interest, located between 0.2 and 1.6 model diameters downstream of the base plane. The decomposition into axial, radial, and tangential vortex components reveals a distinct spatial evolution of the eddy structure. It can be shown that tangential (or toroidal) eddies, initially induced by the shear-layer instability and, thus, having a preferred sense of rotation, gradually break up into three-dimensional structures without favored rotational direction. The current results agree with recent numerical studies that predict comparable features.

Nomenclature

D	=	diameter, m
f	=	focal length, mm
$f/\#$	=	focal ratio
L	=	length, m
Ma	=	Mach number
P	=	first invariant of $\nabla \boldsymbol{v}$, $1/\mathrm{s}$
Q	=	second invariant of $\nabla \boldsymbol{v}$, $1/\mathrm{s}^2$
Re	=	Reynolds number
r	=	radius, m
$\boldsymbol{S}$	=	rate-of-strain tensor, $1/\mathrm{s}$
St	=	Strouhal number
t	=	time, s
U	=	total velocity, m/s
u, v, w	=	velocity components along x, y, z, m/s
x, y, z	=	Cartesian coordinates, m

Greek Symbols

γ	=	correlation coefficient
θ	=	azimuth angle, °
λ	=	eigenvalue of $\nabla \boldsymbol{v}$, $1/\mathrm{s}$
$\boldsymbol{\Omega}$	=	rate-of-rotation tensor, $1/\mathrm{s}$
ω	=	vorticity, $1/\mathrm{s}$

Subscripts

∞	=	freestream conditions
ax	=	axial component
Ci	=	imaginary part of a complex number
Cr	=	real part of a complex number
n	=	normalized
rad	=	radial component
tan	=	tangential component

Special Symbols

$\nabla \boldsymbol{v}$	=	velocity gradient tensor, $1/\mathrm{s}$

I. Introduction

In the wake of bluff bodies, flow separation occurs along with phenomena like recirculation, increased turbulence levels, periodic shedding processes, and low-pressure regions. For flow bodies, which cannot avoid such geometries, base drag and buffeting effects can vitally reduce performance and efficiency. This holds true for axisymmetric, cylindrical bodies placed parallel to freestream direction, like the generic rocket configuration considered in the current work. Similar geometries were studied extensively for subsonic freestream conditions, with early studies concentrating on static or time-averaged quantities [1,2]. Following the evolution of both experimental and numerical methods, the unsteadiness of the wake turned into focus. Many studies reported a macroscopic vortex shedding mode at a reduced frequency of $St_D = 0.2$ [3–5], that was also detected in hot-wire and dynamic base pressure measurements regarding the present case [6]. The instability of the shear layer is assumed to be a key factor in the shedding mechanism and the wake topology [4]. Correspondingly, Pastoor et al. [7] used zero-net-mass-flux actuation to actively manipulate the shear layer of a bluff body over wide Reynolds ranges. A possible overall drag reduction of 15% was reported. Perret [8] investigated the wake of a quasi-two-dimensional (2-D) cylinder by means of two-component (2C) particle image velocimetry (PIV) for $Re_D = 1.25 \cdot 10^5$ [8]. Within the shear layer, a vortex population was detected using the swirling strength criterion. The corresponding structures were both small (<5% of the model diameter) and of high intensity compared to the macroscopic Kármán vortices, and, thus, connected to the Kelvin–Helmholtz instability mechanism. It was also pointed out that for 2-D measurements, only the planar swirling motion can be taken into account and may be affected or biased by the out-of-plane velocity and inclined vortex axes [8].

Fewer results can be found regarding three-dimensional (3-D) test cases. Deck and Garnier [5] performed both detached and large eddy simulations (DES/LES) on the wake flow of a cylindrical, generic launch vehicle model. The bluff base geometry was prolonged by a

Presented at the 41st AIAA Fluid Dynamics Conference and Exhibit, Honolulu, Hawaii, June 27–30, 2011; received 27 November 2011; revision received 10 April 2012; accepted for publication 11 April 2012.

*Research Engineer, Wuellnerstr 7. Member AIAA.
†Senior Research Engineer, Wuellnerstr 7.

second cylinder representing a jet nozzle. Because of its dimensions (length and diameter are 0.6 and 0.4 times the diameter of the forebody), the shear layer emanating from the main body did not reattach to the nozzle. Instantaneous vortex structures were visualized using the Q-criterion and exhibited an evolution from toroidal- to longitudinal-oriented eddies that will, in principle, also be observed in the current study. In a followup paper [9] using zonal DES the nozzle body was elongated to 1.2 times the forebody diameter, approximately corresponding to the Ariane 5 afterbody. Although the shear layer reattached to the nozzle body in this case, its general evolution remained unaffected compared to the case without reattachment. A more detailed analysis of the shear-layer dynamics and the behavior of the instantaneous vortex structures was presented later [10,11], the argumentation will be outlined shortly here. As the experimental results discussed later feature only small subvolumes of the wake, Fig. 1 presents an explanatory instantaneous snapshot of the wake vortex distribution as seen by a detached eddy simulation (DES) of the current case [12], corresponding to Fig. 4 in [10]. The structures can be explained as follows: because of the rollup process of the shear layer (Kelvin–Helmholtz mechanism), the initial stage is governed by toroidal-orientated vortices (T). These structures are ring-like or at least stretch over large azimuthal angles. It is well known that vortex rings are affected by azimuthal instability nodes, which correspond to sinusoidal deflections of the vortex core. The phenomenon was addressed by the pioneering work in [13]. As a consequence of this mechanism, the toroidal eddies are destabilized into hairpin-shaped coherent structures, (H), and general turbulent structures (3-D). In the late stages of the shear layer (near the rearward stagnation point), it seems that the turbulent structures are not completely statistical, but they favor streamwise-aligned, longitudinal vortices (L). An explanation for this behavior can be found in the "tilting and stretching" mechanism, which describes the influence of velocity gradients on the temporal behavior of vortex structures. By taking the curl of the momentum equation one can derive the vorticity transport equation. For incompressible flows and neglecting viscous effects, the radial and axial components in a cylindrical coordinate system are [14]:

$$\frac{D\omega_{\mathrm{rad}}}{Dt} = \underbrace{\omega_{\mathrm{rad}}\frac{\partial v_{\mathrm{rad}}}{\partial r}}_{\text{stretching}} + \underbrace{\omega_{\mathrm{ax}}\frac{\partial v_{\mathrm{rad}}}{\partial x}}_{\text{tilting}} \tag{1}$$

and

$$\frac{D\omega_{\mathrm{ax}}}{Dt} = \underbrace{\omega_{\mathrm{ax}}\frac{\partial u}{\partial x}}_{\text{stretching}} + \underbrace{\omega_{\mathrm{rad}}\frac{\partial u}{\partial r}}_{\text{tilting}} \tag{2}$$

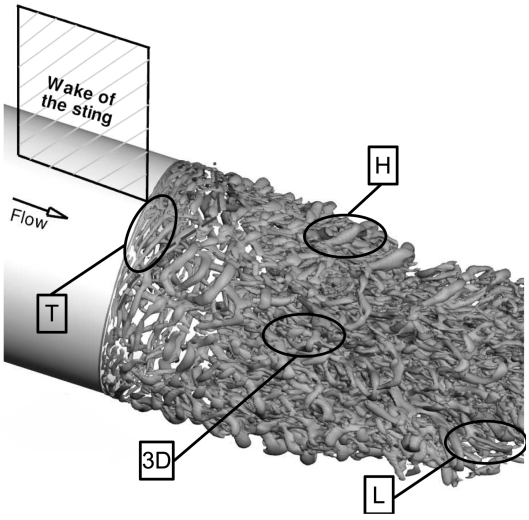

Fig. 1 Vortex structures (Q-criterion) of the current test case as seen by DES [12].

Radial and axial vorticities are denoted by ω_{rad} and ω_{ax}, radial and axial velocity components by v_{rad} and u, and radial and axial coordinates by r and x, respectively. The first term on the right side of each equation illustrates the "vortex stretching", describing the attenuation or amplification of vorticity through a velocity gradient along the same spatial direction. The second term represents the "vortex tilting" that is the exchange between the axial and radial vorticity under the influence of perpendicular velocity gradients. For the shear layer of an axisymmetric near wake, it is obvious that the gradient of axial velocity along radial position, $\partial u/\partial r$, outweighs the gradient of radial velocity along axial position, $\partial v_{\mathrm{rad}}/\partial x$. Hence, it is more likely that radial eddies are tilted in the axial direction than vice versa, explaining a predominant occurrence of longitudinal eddies in the developed shear layer.

The main objective of the present study is to provide data on vortex structures in a bluff-body wake flow with high spatial resolution. In particular, the focus lies on finding experimental proof for the breakup and reorganization process of the vortex structures elucidated in the previous section. The work is part of the German Collaborative Research Center SFB-TR40: "Technological foundations for the design of thermally and mechanically highly loaded components of future space transportation systems." A subdivision of this center is dedicated to wake flow investigations, given that wake issues (especially base buffeting) are of great importance for current launcher systems [15]. Starting with a common set of model configurations, the base flow is investigated in subsonic [16,17], transonic [17], and supersonic/hypersonic regimes [17,18]. One of the main goals of the experimental work is to provide data that feed into the development of high-fidelity computational fluid dynamics code, like DES or Reynolds averaged Navier-Stokes/LES hybrid methods. To overcome the aforementioned limitations of many preceding experimental studies, Tomo-PIV is applied. This methodology enables the determination of instantaneous three-component (3C) velocity vectors in a 3-D measurement volume. It should be mentioned that a limited number of former investigations used different PIV techniques to acquire the complete velocity gradient tensor $\nabla \boldsymbol{v}$, including dual-plane PIV, holographic PIV, or cinematographic stereoscopic PIV. Advantages and limitations of these methods were summarized in [19]. Despite being an innovative technique, Tomo-PIV already demonstrated its capability of detecting turbulent structures considering different applications. Haigermoser et al. [20] used this measurement technique to characterize the turbulent flow over a circular cavity, concentrating on velocity fluctuations and instantaneous vortical formations [20]. Schäfer et al. [21] were able to experimentally prove a new concept of turbulence characterization, the theory of dissipation elements, in good agreement to direct numerical simulation. However, publications that draw quantitative conclusions from the enhanced capabilities of volumetric PIV are still rare, partly as a consequence of the complex and time-consuming measurement techniques that are involved.

The model geometry and the experimental setup of the current measurements are introduced in Secs. II and III, respectively. The vortex identification criteria and the corresponding mathematical background is outlined in Sec. IV. Section V presents the results of this investigation and is subdivided into three parts. First, the Tomo-PIV results are compared to standard PIV techniques. Second, a vortex onset threshold is proposed to differentiate between flow structures and measurement noise. The last part performs a statistical analysis to evaluate the spatial evolution of the shear layer.

II. Model Geometry

The model consists of a cylindrical main body with blunt base geometry and an adjoined conical nose section, which accounts for an overall length-to-diameter ratio of 10. The sting support is covered by an unswept NACA-profiled fairing attached to the main body at an upstream position to minimize its influence on the base flow. Further details on the geometry can be taken from Fig. 2. In later phases of this project, a nozzle with jet flow simulation will be integrated to enhance the relevance of the experiments considering space launcher

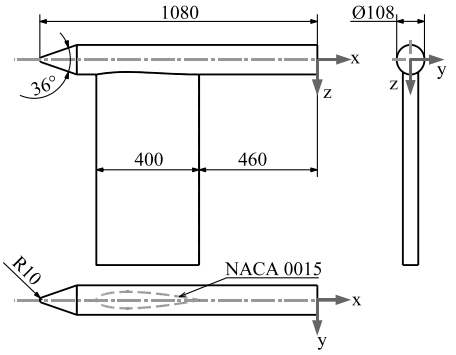

Fig. 2 Model geometry (dimensions in mm).

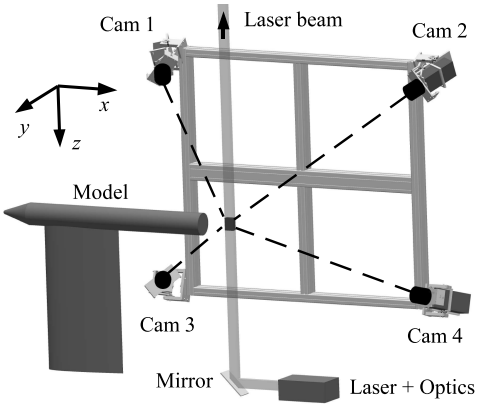

Fig. 3 Sketch of the optical setup.

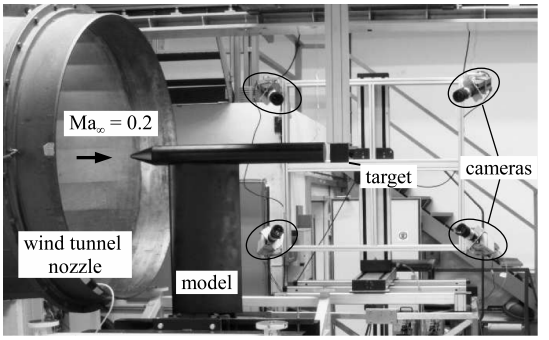

Fig. 4 Wind tunnel assembly.

geometries. In the current, most generic layout, the results may be transferred to a wide range of subsonic applications. To ensure a turbulent boundary layer with defined transition, a trip wire (0.8-mm-diam) was applied to the nose cone, which is 0.45 model diameters downstream of the tip. Transition was verified in preliminary surface oil-flow experiments. The model was integrated into the open test section of a closed-circuit wind tunnel operated at $Ma_\infty = 0.2$, resulting in a Reynolds number of $Re_D = 4.4 \cdot 10^5$. The diameter of the wind tunnel nozzle is 1.5 m, yielding a low area blockage ratio below 3%. The open test section has a length of 3 m and results in a comparably high freestream turbulence level (about 2.5%), but on the other hand provides excellent optical access for the sophisticated camera setup.

III. Experimental Setup

Instantaneous snapshots of the 3-D flowfield were captured using Tomo-PIV. A detailed description of the working principle is given in [22] and will only be summarized briefly. The airflow was seeded with vaporized Di-Ethyl-Hexyl-Sebacat oil droplets serving as tracer particles. A double-pulsed, frequency-doubled Nd:YAG laser providing a pulse energy of 120 mJ illuminated the measurement volume. The separation time between double frames was set to 8 μs. The width and height of the laser beam's cross section were expanded separately, in each case using a pair of cylindrical lenses ($f = -25/150$ mm and $f = -50/200$ mm) providing a nearly collimated beam. After passing a rectangular aperture, the laser cross profile covered approximately 34 by 13 mm. Particle images were taken from four different viewing angles using PIV cameras mounted on a common frame. Each line of sight enclosed an angle of approximately 40 deg to the face normal of the measurement volume; the viewing distance was about 1.6 m. Gimbaled lens mounts providing dual axis of rotation were designed to meet the Scheimpflug criterion in 3-D space, which kept the entire volume in focus. The calibration of the camera system was accomplished using a two-level precision target that was traversed throughout the depth of the measurement region. Additional information on the camera setup is given in Table 1. The maximum repetition rate of the cameras is 5 Hz, preventing time-resolved measurements of the base flow.

A conceptual sketch of the PIV setup including model, light source, and camera assembly is depicted in Fig. 3. The laser beam was reflected by an adjustable mirror and crossed the measurement volume from bottom to top. Target, cameras, and the laser were mounted on individual traverse systems for convenient and precise translation of the measurement volume (see Fig. 4). Using particle images from different viewing angles, the 3-D positions of the tracer particles were reconstructed using an iterative MART algorithm [23]. For this procedure, the allowable maximum calibration error is typically in the order of 0.1 pixel and, thus, much lower compared to standard PIV methods. During experiments, slight camera vibrations were excited by both ground vibrations originating in the tunnel motor and unsteady aerodynamic loads within the open test section. As a countermeasure, the calibration was corrected for each double-frame image pair by the triangulation of particle positions between each camera. The corresponding reconstructions are of similar quality compared to measurements avoiding camera vibrations through significantly lower freestream velocity. Details on the calibration correction were described in [24] and will not be discussed further in this article.

Particle shifts within the reconstructed volume and, thus, the local flow velocity were determined by an iterative, adaptive cross-correlation algorithm, which is a straightforward extension to planar counterparts used in standard PIV evaluation. The final interrogation windows after three correlation passes were sized $42 \times 42 \times 42$ pixel^3 with an overlap of 75%, providing a spacing of 2.2 vectors per mm. For the given dimensions and resolution, each flowfield contains more than $2 \cdot 10^5$ grid points. Spatial derivatives were calculated using a second-order central-difference scheme in Cartesian coordinates, providing $\nabla \boldsymbol{v}$. Because of high-computational demands of the volumetric reconstruction the number of samples recorded for each volume had to be limited to 600. Commercial software, LaVision DaVis 8, was used for calibration, volume reconstruction, and cross correlation. Further evaluations including the calculation of velocity gradients and vortex criteria, vortex identification, statistical postprocessing, and visualization were accomplished by the development of in-house code based on MATLAB.

The cross section of the volumetric results is slightly smaller (about 30 mm $\times$ 11 mm) compared to the laser cross section due to a

Table 1 Camera setup for Tomo-PIV

Camera no.	Camera type	Operation mode	Sensor size	f	$f/\#$	Resolution
1, 2	PCO pco.2000	Forward scatter	2048 $\times$ 2048 px^2	200 mm	8	18 . . . 20 px/mm
3, 4	PCO sensicam.qe	Backward scatter	1376 $\times$ 1040 px^2	180 mm	8	18 . . . 20 px/mm

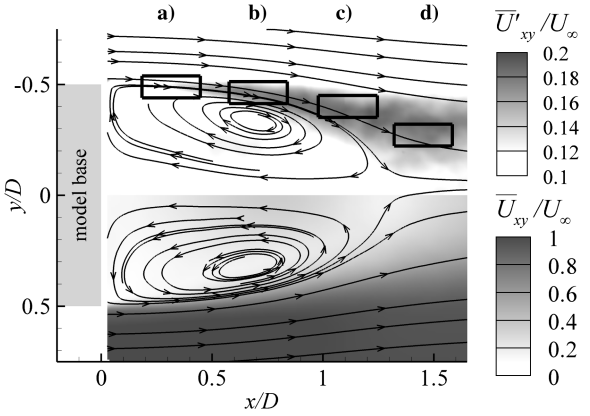

Fig. 5 Base flow and Tomo-PIV cross sections.

diminishing signal-to-noise ratio at the boundaries. The height of the volume (along the laser beam path) is about 56 mm, limited by the field of view of cameras 3 and 4. The current investigation covers four measurement regions, which are labeled A, B, C, and D. The positions were selected to follow the evolution of the shear layer that develops between external flow and base flow. Figure 5 outlines the volumes' location in the horizontal x–y-plane. For reference, the graphic also includes planar streamlines, the average of the planar velocity $U_{xy} = (u^2 + v^2)^{0.5}$ (lower half), and the corresponding turbulence level (upper half) as seen by preliminary 2C-PIV experiments. The $x/y/z$ positions of the volumes are summarized in Table 2.

IV. Mathematical Description of the Vortex Structures

In the past decades, a variety of identification schemes were developed to detect instantaneous vortical structures in flowfields. The majority of the related publications agree that an appropriate criterion needs to be Galilean invariant and, thus, independent of the convection velocity of the vortex core [25]. In addition, the streamlines must exhibit a spiraling motion within the reference frame defined by the vortex core. For example, this implicitly rules out the consideration of the vorticity, which is not only sensitive to eddies but also to shear stresses. Many criteria are based on a local approach evaluating the velocity gradient tensor $\nabla \boldsymbol{v}$. The present work follows the argumentation of two common criteria: the Q-criterion in [26] and the λ_{Ci}-criterion in [27]. Not considered here, but also frequently applied are the Δ- and λ_2 approaches. A detailed comparison of the different vortex criteria, including Q and λ_{Ci}, can be found in [28].

A. Q-Criterion

In the most universal formulation of the Q-criterion, the scalar quantity Q' is defined as the second invariant of $\nabla \boldsymbol{v}$:

$$Q' = \frac{1}{2}(P^2 + \|\boldsymbol{\Omega}\|^2 - \|\boldsymbol{S}\|^2) \tag{3}$$

P denotes the first invariant of $\nabla \boldsymbol{v}$, whereas $\boldsymbol{S}$ and $\boldsymbol{\Omega}$ mark the symmetric and antisymmetric part of $\nabla \boldsymbol{v}$, respectively:

$$P = -\nabla \cdot \boldsymbol{v} = -\left(\frac{\partial u}{\partial x} + \frac{\partial v}{\partial y} + \frac{\partial w}{\partial z}\right) \tag{4}$$

Table 2 Position of Tomo-PIV-volumes

Volume	x/D	y/D	z/D
A	0.18…0.45	−0.54 … − 0.44	−0.27 … 0.27
B	0.57…0.84	−0.51 … − 0.41	−0.26 … 0.26
C	0.98…1.25	−0.45 … − 0.35	−0.27 … 0.27
D	1.32…1.58	−0.32 … − 0.22	−0.28 … 0.28

$$\boldsymbol{S} = \frac{1}{2}(\nabla \boldsymbol{v} + \nabla \boldsymbol{v}^T) \tag{5}$$

$$\boldsymbol{\Omega} = \frac{1}{2}(\nabla \boldsymbol{v} - \nabla \boldsymbol{v}^T) \tag{6}$$

In this equation, $\|\cdot\|$ denotes the Frobenius norm. For subsonic conditions at $Ma_\infty = 0.2$, P can be omitted from Eq. (3) as a consequence of incompressibility. In this case, Q represents the excess of the rate of rotation $\|\boldsymbol{\Omega}\|$ over the rate of strain $\|\boldsymbol{S}\|$:

$$Q = \frac{1}{2}(\|\boldsymbol{\Omega}\|^2 - \|\boldsymbol{S}\|^2) \tag{7}$$

For experimental data, P will most likely deviate from zero to a certain degree due to the uncorrelated measurement noise affecting the determination of the velocity gradients. Hence, the average value of P can be considered as a measure for the noise level. With respect to Eq. (3), the ratio between $\|\boldsymbol{\Omega}\|^2 - \|\boldsymbol{S}\|^2$ and P^2 can be interpreted as a signal-to-noise ratio, as it compares the vortex strength to the noise level. Consequently, using Eq. (7),

$$\frac{\|\boldsymbol{\Omega}\|^2 - \|\boldsymbol{S}\|^2}{P^2} = \frac{2 \cdot Q}{P^2} \tag{8}$$

A similar approach to the determination of measurement noise is presented in [19]. In this case, the probability density of the normalized divergence error $\nabla \cdot \boldsymbol{v}/\|\nabla \boldsymbol{v}\|$ is evaluated.

B. λ_{Ci}-Criterion

The λ_{Ci}-criterion, also referred to as "swirling strength", identifies regions of spiraling flow through the occurrence of complex conjugated eigenvalues concerning $\nabla \boldsymbol{v}$. Thus, the vortex strength can be connected to the value of the corresponding imaginary part:

$$\lambda_{Ci} = \text{image}(\text{eig}(\nabla \boldsymbol{v})) \tag{9}$$

This quantity may be decomposed into a Cartesian coordinate system by the evaluation of 2-D subsets of the velocity gradient tensor, corresponding to x, y, and z directions. In this case, the information on the sense of rotation may be added by multiplying the 2-D swirling strength with the sign of the corresponding vorticity. For example, regarding x direction, this yields

$$\lambda_x = \text{sign}(\omega_x) \cdot \text{image}(\text{eig}(\nabla \boldsymbol{v}_x)) = \text{sign}\left(\frac{\partial w}{\partial y} - \frac{\partial v}{\partial z}\right) \cdot \text{image}\left[\text{eig}\begin{pmatrix} \frac{\partial v}{\partial y} & \frac{\partial v}{\partial z} \\ \frac{\partial w}{\partial y} & \frac{\partial w}{\partial z} \end{pmatrix}\right] \tag{10}$$

Similar equations can be formulated for y and z directions. Additionally, the Cartesian velocity components may be transferred into a cylindrical coordinate system reflecting the axisymmetric model geometry. This results in axial, radial, and tangential components. To ensure comparability to other investigations and model geometries the following normalizations have been applied, denoted by the index n:

$$Q_n = Q \cdot D^2 \cdot U_\infty^{-2} \quad \text{and} \quad \lambda_n = \lambda \cdot D \cdot U_\infty^{-1} \tag{11}$$

V. Results

A. Comparison to Standard Particle Image Velocimetry Techniques

Figure 6 compares a randomly chosen instantaneous sample of volume B (left) to the corresponding average velocity distribution (right), calculated from a total of 600 instantaneous samples. The mean distribution obviously illustrates a cutout of the toroidal wake area, whereas the instantaneous counterpart gives a first impression of the turbulence involved in the shear layer. Because Tomo-PIV is a both innovative and complex measurement technique, the results

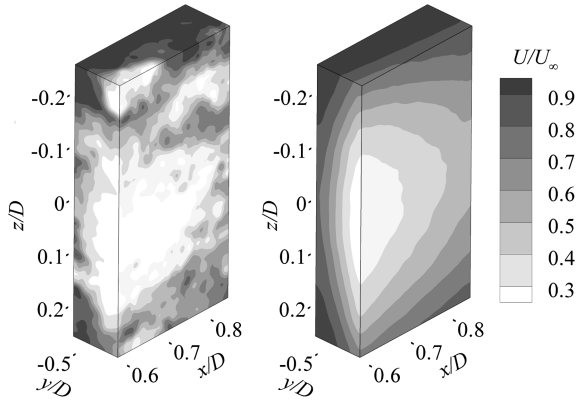

Fig. 6 Instantaneous (left) and averaged (right) flowfield.

were verified using data taken from preliminary, well-established planar PIV measurements. The corresponding geometry, e.g., for Tomo-PIV volume B, is exemplarily depicted in Fig. 7. Each Tomo volume intersects two planar regions of interest in a common sectional plane, for which the mean velocity and mean fluctuation levels can be compared. 2C-PIV was applied in the horizontal plane ($z = 0$), corresponding to the results already presented in Fig. 5, allowing for a comparison of the planar velocity $U_{x,y}$ and the corresponding turbulence levels. In contrast, several planes perpendicular to freestream direction (in this case located at $x/D = 0.68$) require 3C-PIV due to the nonnegligible out-of-plane velocity, allowing for the evaluation of the value of the 3-D velocity vector U. Both 2C and 3C measurements feature a lower spatial resolution (0.8 and 0.6 vectors per mm), hence, the Tomo-PIV data (2.2 vectors per mm) was interpolated to a common, coarser grid. In all three cases, a comparable number of flowfields (450 to 600 samples) was taken into account for a statistical analysis.

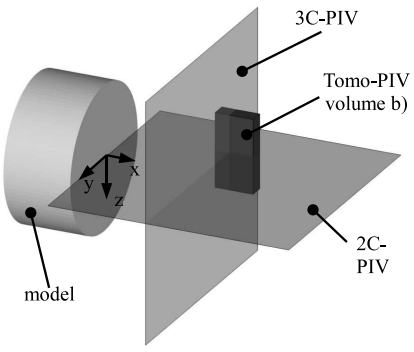

Fig. 7 Intersection planes.

For example, a comparison of Tomo-volume B and 3C-PIV reveals a reasonable good agreement, as both mean velocity and turbulence levels exhibit very similar distributions, see Figs. 8a and 8b. The relative deviations stated hereafter are referenced to the freestream velocity U_∞. The average deviation regarding mean velocity, $(\bar{U}_{\text{Tomo}} - \bar{U}_{3C})/U_\infty$, is -2.8%, compared to the average deviation regarding turbulence level, $(\bar{U}'_{\text{Tomo}} - \bar{U}'_{3C})/U_\infty$, which is $+2.4\%$. The value of the corresponding maximum deviations occurring in the intersection plane are 6.2 and 4.1%, respectively. For a similar comparison of Tomo-volume B and 2C-PIV (not shown), even lower discrepancies are observed.

A comprehensive overview of the comparisons performed for all volumes A to D is presented in Table 3. The results are summarized by the following statements: regarding mean velocities, average discrepancies up to 5% (typically $< 3\%$) are observed. This level of confidence was expected and corresponds to the deviations that are observed between both standard PIV techniques (2C/3C). It has to be emphasized that in the measurement volumes, the shear layer exhibits a very steep velocity gradient of up to 6% per mm. Hence, the observed deviations can be evoked by misalignments of the calibration target smaller than 0.5 mm. This mechanism is supposed to be one of the primary error sources. Furthermore, Tomo-PIV turbulence levels agree well with 2C-PIV (mean deviations lower than 0.6%), but show systematically higher values compared to 3C-PIV (mean deviations up to $+2.5\%$). In general, there are three main reasons that may explain this deviation. First, in this case Tomo-PIV has a superior resolution compared to 3C-PIV, which enables Tomo-PIV to capture smaller-scaled structures and, thus, a higher percentage of the turbulence cascade. Second, the velocity distribution determined using standard PIV is inherently averaged over the thickness of the laser light sheet (approximately 5 mm in this case). This especially concerns the 3C measurements, as the light sheet is perpendicular to the main flow directon. Third, turbulence levels of Tomo-PIV may be affected by increased measurement noise compared to standard PIV due to the different working principle, e.g., the additional step of volumetric reconstruction. Thus, a detailed investigation on the measurement noise will be given in the following chapter.

B. Vortex Onset Threshold and Instantaneous Flowfields

In the narrower sense, a vortex region is defined by either $Q_n > 0$ or $\lambda_{Ci,n} > 0$, depending on the chosen criterion. A nonzero threshold may be applied to concentrate on the most significant structures only and to separate flow features from background noise. In this context, Perret [8] determines the background noise of the applied 2C-PIV system through comparative measurements of a wind tunnel test section with a negligible freestream turbulence level. In this case, the cutoff noise level is estimated to $\lambda_{Ci,n} = 2.2$.

As the freestream turbulence is not negligible in the present case, a different approach is introduced. The following considerations refer

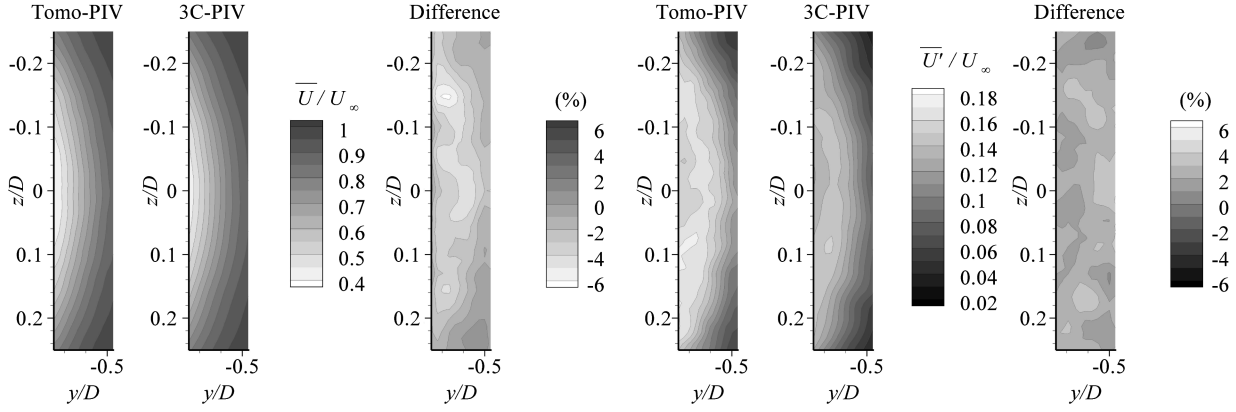

a) Average velocity **b) Turbulence level**

Fig. 8 Comparison of Tomo-PIV volume B and 3C-PIV.

Table 3 Average deviations between Tomo- and standard-PIV

	Pos. intersect. plane		Diff. mean level, $\%U_\infty$		Diff. turb. level, $\%U_\infty$	
Volume	2C, z/D	3C, x/D	$\bar{U}_{\text{Tomo}} - \bar{U}_{2C}$	$\bar{U}_{\text{Tomo}} - \bar{U}_{3C}$	$\bar{U}'_{\text{Tomo}} - \bar{U}'_{2C}$	$\bar{U}'_{\text{Tomo}} - \bar{U}'_{3C}$
A	0	0.23	2.9	−5.2	0.6	1.9
B	0	0.68	0.9	−2.8	0.3	2.4
C	0	1	−0.6	−4.6	0.1	2.5
D	0	—	−2.9	—	−0.1	—

to the dataset of volume A, in total representing more than 10^8 data points (600 samples with each $>2 \cdot 10^5$ velocity vectors). The solid graphs in Fig. 9 depict the vortex density as a function of the threshold choice for Q_n (top) and $\lambda_{Ci,n}$ (bottom). "Vortex density" is defined as the average percentage of a flowfield belonging to a vortical region. For the threshold choices $Q_n = 0$ and $\lambda_{Ci,n} = 0$, the vortex densities are about 35 and 70%, respectively. In this case, both criteria obviously yield very different results. Following the argumentation in [28], regions satisfying $Q > 0$ are always a subset of regions for $\lambda_{Ci} > 0$, excluding areas with a significant stretch or compression of the vortex axis ($|\lambda_{Cr}/\lambda_{Ci}| > 1/\sqrt{3}$). Despite this physical interpretation, synthetic tests showed that the $\lambda_{Ci} > 0$-condition is also more sensitive towards noise corrupting the velocity gradient tensor. With an increasing threshold both criteria expectedly identify less vortices and, thus, exhibit a lower vortex density. For small positive values, both graphs exhibit a steep gradient indicating a high sensitivity in this area. For higher thresholds, the identified structures become more independent from the threshold choice.

For additional insight, two subvolumes are extracted from measurement volume A: one represents a turbulent region within the shear layer (Fig. 9, dashed graphs), whereas the other subvolume is situated in the external flow (Fig. 9, dotted graphs). For $Q_n = 0$ and $\lambda_{Ci,n} = 0$, both subvolumes approximately exhibit the same vortex density, which is questionable due to the different flow regimes. For positive thresholds, an increasing margin between both flow regions can be observed, as the vortex density decreases much faster in case of the external flow. The greatest difference is observed around $Q_n = 20$ and $\lambda_{Ci,n} = 3.5$, respectively.

Figure 10 depicts isosurfaces of the quantities Q_n and $\lambda_{Ci,n}$ for an exemplary instantaneous flowfield. To improve the clarity of the graphs and to remove artifacts the distributions were smoothed using a Gauss filter in a 3^3 neighborhood. The ability to identify small-scale coherent structures is limited by the depth of the volume ($\Delta y = 0.1 \cdot D$) and the spatial resolution. The expected core radius of shear-layer vortices is typically around $0.02 \cdot D$ [8], suggesting that the dimensions of the chosen measurement regions are appropriate. Yet it should be noted that each volume contains between 24 and 26 velocity vectors along y axis, with only every fourth vector statistically uncorrelated due to the correlation overlap of 75%. For zero threshold choices, $Q_n = 0$ and $\lambda_{Ci,n} = 0$ (not shown), the isosurfaces exhibit a very turbulent and/or noisy layout with no distinct coherent structures. When choosing a nonzero threshold of $Q_n = 20$ (Fig. 10, left), corresponding to the maximum differentiation between shear layer and external flow as seen in Fig. 9, filamentous or tube-like structures can be identified. Comparable structures were shown before in similar studies [5,10]. The average vortex density of $Q_n = 20$ is about 15%, which corresponds a normalized value of 6.5 regarding λ_{Ci}-criterion. The associated isosurfaces (Fig. 10, right) show a very good agreement to the Q-criterion, which becomes most apparent in two ring-like structures that are encircled in both illustrations.

Although it is not expected that both Q- and λ_{Ci}-criteria are exactly identical [28], statistics reveal that the correlation coefficient γ between Q_n and $\lambda_{Ci,n}$ is always above 0.9 and exhibits an ascending trend for increasing Q-thresholds (Fig. 11, left). In contrast, the quantity Q is only slightly correlated to the noise-induced $0.5 \cdot P^2$, as the corresponding γ assumes small positive values below 0.3, also see Fig. 11. This explains a growth of the averaged signal-to-noise ratio defined by Eq. (8) for increasing values of the threshold Q_n, see Fig. 11, right.

Given the results presented in Fig. 11, an appropriate value for the vortex onset threshold can also be determined by linking the threshold value to the noise level of the measurements, e.g., setting the threshold for Q to the average value of the noise-induced $0.5 \cdot P^2$ yields a normalized value of 16, which is close to the value of 20 that was found in the previous section using a different argumentation. Both thresholds can be exchanged without affecting the main conclusions of this paper.

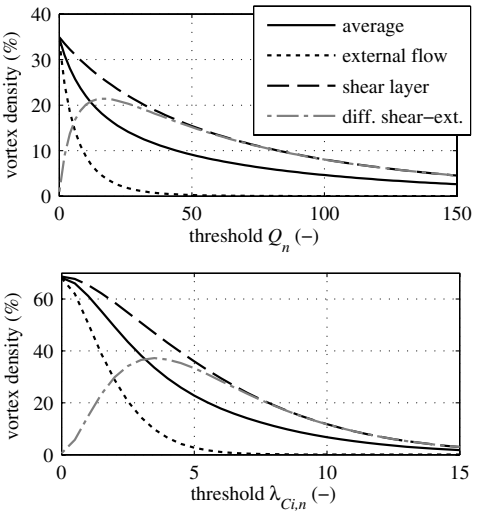

Fig. 9 Vortex density versus threshold choice.

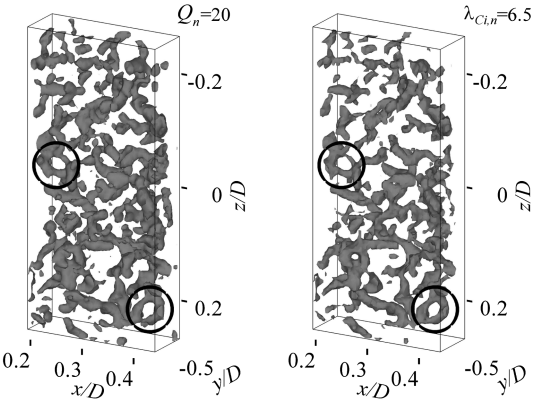

Fig. 10 Isosurfaces for Q and λ_{Ci}-criterion.

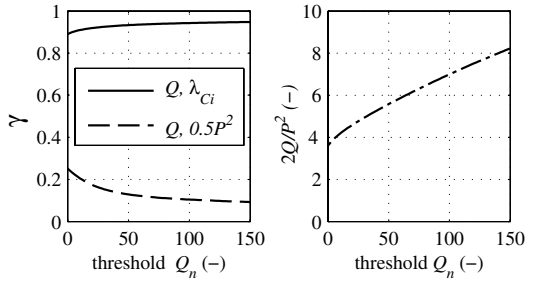

Fig. 11 Correlation coefficient and signal-to-noise ratio.

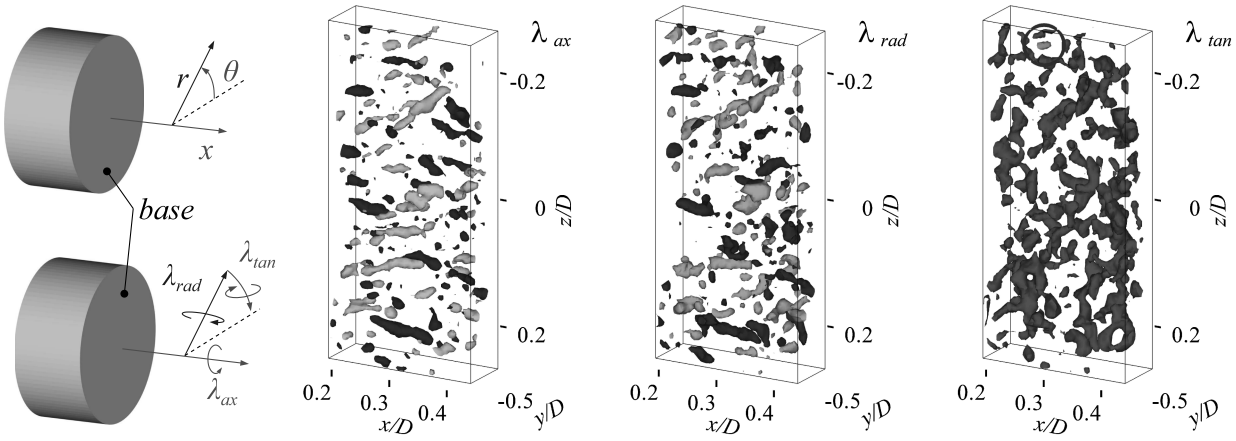

Fig. 12 Axial, radial, and tangential components: light shades $\lambda < 0$, and dark shades $\lambda > 0$.

In summary, an appropriate vortex onset threshold is useful to isolate vortical structures within the shear layer and to suppress measurement noise. To identify eddy structures in 3-D space, both Q- and λ_{Ci}-criteria may be applied and yield similar results. For further considerations, the condition $\lambda_{Ci,n} \geq 6.5$ will be chosen over the Q-criterion, as the λ_{Ci}-criterion can be easily decomposed into 2-D representations. It should be noted that this threshold choice is about three times higher compared to standard PIV measurements conducted in [8] in a less turbulent environment.

C. Statistical Analysis

Once vortical regions are identified, the corresponding swirling motion may be decomposed into Cartesian coordinates and further transformed into cylinder coordinates. In this context, Fig. 12 depicts regions with prevailing axial, radial, or tangential component for the ($\lambda_{Ci} \geq 6.5$) structures that were discussed prior in Fig. 10, right. With respect to Eq. (10), the 2-D swirling strength can assume negative and positive values, which is illustrated by light and dark shading, respectively. In this example, the positive and negative senses of rotation are rather balanced for axial and radial components, whereas tangential components favor positive values. A single negative tangential spot can be observed near the top of the volume and has been marked for visualization reasons. Comparing axial, radial, and tangential structures in Fig. 12, it is apparent that many structures appear in more than one view, representing inclined vortices. This is expected, as it is unlikely that turbulent structures are perfectly aligned along the cylindrical axes. The overlay of all three views yields the 3-D representation that is shown in Fig. 10, right. As it is difficult to extract the evolution of the shear layer from instantaneous samples of the flowfield, a statistical analysis was performed using the following methodology: at first, vortical regions were identified in 3-D space for each instantaneous sample, followed by a decomposition into cylindrical components. Afterwards, an averaging was performed for all vortex events of a given grid point. Regarding the vortex density of the chosen threshold and the number of available samples (600), about 90 events per grid point were taken into account. To further reduce the variation throughout the volume, the quantities were averaged over two of three spatial directions.

In a first step, the evolution of the shear layer versus streamwise position x (distance to base) is investigated. Figures 13 and 14 present

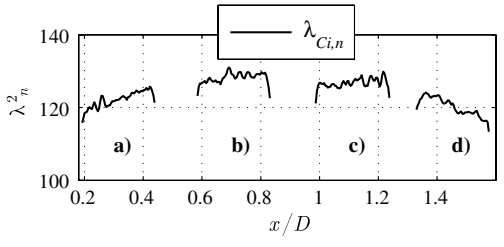

Fig. 13 Averaged 3-D swirling strength versus x coordinate.

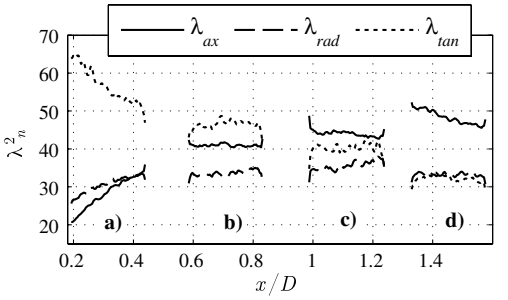

Fig. 14 Averaged decomposed swirling strengths versus x coordinate.

the averaged values of the squared swirling strengths, λ^2, as a measure of the vortex intensity regardless its sense of rotation. In contrast, Fig. 15 depicts the average senses of rotation regardless vortex strength, $\lambda/|\lambda|$, which equal the average signs of the corresponding vorticities [see Eq. (10)] on a scale between -1 and 1. The 3-D swirling strength, λ_{Ci}, is almost independent of the x position (Fig. 13), with a range between 115 and 130 normalized units. Highest values are by tendency located in the middle of the x range, volumes B and C, corresponding to the relatively high-turbulence levels in this area (compare Fig. 5). A close look reveals steep, unphysical slopes of the swirling strength at both up and downstream end of each measurement volume (first and last two to three grid points). It is a well-known problem of PIV that the results become inaccurate at the region of interest's boundary, as the correlation windows (or, in case of Tomo-PIV, correlation volumes) partially overlap the image borders. In contrast to λ_{Ci}, the decomposed swirling strengths $\lambda_{ax,rad,tan}$ are subject to distinct changes along x.

At the most upstream position, $x/D = 0.19$, the tangential component has a dominating influence, with its squared strength surpassing both axial and radial component by a factor of about 2.5 (Fig. 14). In the course of volume A, the tangential component decreases, whereas both radial and axial components simultaneously increase, indicating a reorganization process of the eddy structure towards 3-D structures. Tangential vortex events clearly favor a

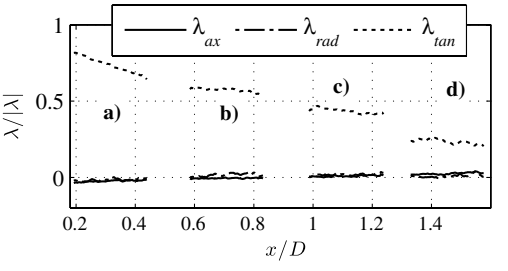

Fig. 15 Averaged vortex sense of rotation versus x coordinate.

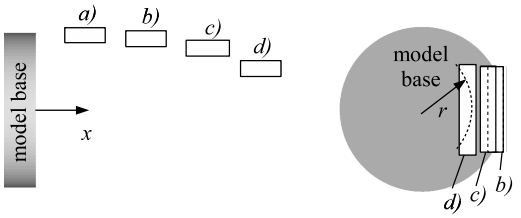

Fig. 16 Axial and radial position of volumes B, C, and D.

positive sense of rotation, with a $(\lambda/|\lambda|)_{\tan}$-value of up to 0.8 (Fig. 15). Given the definition of the coordinate transformation (Fig. 12, left) this sense of rotation complies to instabilities induced by the shear-layer velocity profile. In contrast, axial and radial components exhibit no preferred rotational sense. This result is expected, as a mean swirl along these directions contradicts a rotationally symmetric flowfield. Even though DES calculations on the current geometry in [12] show that the wake of the sting support amplifies the rollup mechanism of the shear layer and, thus, introduces asymmetries, the positioning of the Tomo-PIV volumes avoids the immediate wake region of the sting. Unfortunately, the measurement region could not be extended further upstream towards $x/D = 0$ due to laser light reflections at the base. However, the evolution discussed for volume A suggests that eddies initially originate in tangentially-orientated structures induced by shear stresses, e.g., the Kelvin–Helmholtz mechanism, and, thus, having a corresponding sense of rotation.

The evolution in volumes B, C, and D can be summarized as follows: the squared swirling strength of the radial component remains nearly constant for $0.58 \geq x/D \geq 1.58$. Axial components gradually gain in importance, whereas the tangential component further diminishes until in volume D reaching the level of radial vortices. At the most downstream position, $x/D = 1.58$, the ratios $\lambda^2_{\tan}/\lambda^2_{\text{ax}}$ and $\lambda^2_{\text{rad}}/\lambda^2_{\text{ax}}$ account for about 0.66, indicating that axial vortices predominate late stages of the shear layer. The rotational preference of tangential vortices towards positive values also subsequently decreases, reaching a near-balanced level of 0.2 at volume D. Considering Fig. 14 it is apparent that only the quantities in volume A exhibit a steady evolution along x. For volumes B, C, and D, the swirling strengths seem rather constant across each volume but shift in between, yielding a "staircase"-shaped appearance. This behavior will be explained in the following section.

For an axisymmetric geometry, the statistical flow properties are independent of the azimuth angle θ. This leaves the radial distance r as the second spatial variable next to x having a possible influence on the vortex structure. Given the rectangular cross section of the measurement regions (see Fig. 16), only a small radial range is covered by each volume, making it difficult to draw corresponding conclusions. Figures 17 and 18 depict the decomposed, averaged vortex strengths and senses of rotation as function of r, using nine sampling points for each measurement region B, C, and D. In these representations, the reorientation from tangential to axial structures and the near-constant swirling strength of radial eddies is reproduced for decreasing radii. The steady decay in the rotational preference of tangential vortices is also confirmed for a decreasing radial

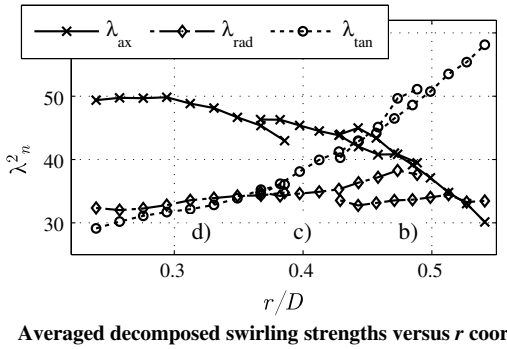

Fig. 17 Averaged decomposed swirling strengths versus *r* coordinate.

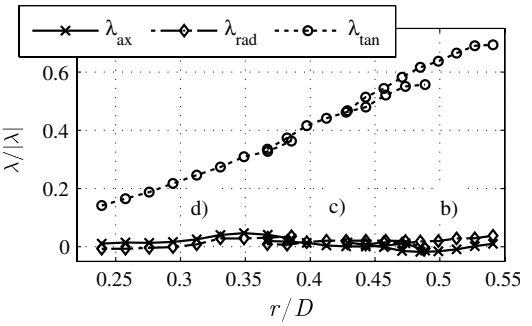

Fig. 18 Averaged vortex sense of rotation versus *r* coordinate.

coordinate. When evaluated as function of r instead of x, the swirling quantities exhibit a much steadier evolution in this area. Also, the overlapping or transition areas between neighboring volumes now show a rather continuous behavior, supporting the assumption that r is the main cause variable in this area.

VI. Conclusions

The shear layer of an axisymmetric, bluff-body wake flow was investigated using the innovative Tomographic particle image velocimetry (PIV), providing volumetric data on instantaneous flowfields. The ability to capture the corresponding flow features was demonstrated by comparison with well-established standard PIV techniques, yielding a satisfying agreement. Vortical structures were identified using both Q- and λ_{Ci}- criterion. It was shown that an appropriate vortex onset threshold is required to isolate large-scale coherent structures and to dampen measurement noise. The clarity of the visualization regarding isosurfaces of Q- and λ_{Ci}-levels was improved by applying Gauss filtering. A statistical evaluation reveals that the initial structures are dominated by tangentially orientated eddies with strong rotational preference. After a gradual breakup into three-dimensional (3-D) structures the final stages of the shear layer are predominantly governed by axial vortices without preferred sense of rotation. This evolution is both dependent on the axial position (early stages), as well as on the radial position (later stages). The results qualitatively comply to recent computational fluid dynamics simulations, which investigate similar model geometries. A quantitative comparison to a high-fidelity detached eddy simulation (DES) on the current configuration is planned for the future. A topic that still needs to addressed is the boundary effect that occurs at the borders of each measurement volume. Also, it is desirable to study the vortex evolution covering an increased radial range.

This would greatly benefit from larger measurement volumes, which were limited in the present case due to the available laser light energy and camera resolution.

Acknowledgments

Financial support has been provided by the German Research Foundation in the framework of the Sonderforschungsbereich Transregio 40. The authors thank Dirk Michaelis of LaVision, Göttingen, for the development of the Single Image Volume Self Calibration algorithm for Tomographic particle image velocimetry (Tomo-PIV). Detached eddy simulation (DES) results on the wake flow were provided by Yancheng You of the German Aerospace Centre (DLR), whose support is greatly appreciated.

References

[1] Merz, R., Page, R., and Przirembel, C., "Subsonic Axisymmetric Near-Wake Studies," *AIAA Journal*, Vol. 16, No. 7, 1978, pp. 656–662. doi:10.2514/3.60954

[2] Buresti, G., Fedeli, R., and Ferraresi, A., "Influence of Afterbody Rounding on the Pressure Drag of an Axisymmetric Bluff Body," *Journal of Wind Engineering and Industrial Aerodynamics*, Vols. 69–71, July–Oct. 1997, pp. 179–188. doi:10.1016/S0167-6105(97)00153-0

[3] Deprés, D., and Reijasse, P., "Experimental Study of Wall Pressure in

Afterbody Flows With and Without Jet," AIAA Paper 2003-3469, June 2003.

[4] Kawai, S., and Fujii, K., "Time-Series and Time-Averaged Characteristics of Subsonic to Supersonic Base Flows," *AIAA Journal*, Vol. 45, No. 1, 2007, pp. 289–301. doi:10.2514/1.24601

[5] Deck, S., and Garnier, E., "Detached and Large Eddy Simulation of Unsteady Side-Loads over an Axisymmetric Afterbody," *Proceedings of the 5th European Symposium on Aerothermodynamics for Space Vehicles*, ESA-SP563, The European Space Agency, Noordwijk, The Netherlands, 2005.

[6] Wolf, C. C., Henke, R., and Hörnschemeyer, R., "Investigation on Turbulence Properties in the Wake of a Generic Rocket Model," Sonderforschungsbereich/Transregio 40—Annual Report 2010, 2010, pp. 99–108, http://www.sfbtr40.de/images/stories/annualreport2010/b2%20investigation.pdf [retrieved 10 April 2012].

[7] Pastoor, M., Henning, L., Noack, B. R., King, R., and Tadmor, G., "Feedback Shear Layer Control for Bluff Body Drag Reduction," *Journal of Fluid Mechanics*, Vol. 608, Aug. 2008, pp. 161–196. doi:10.1017/S0022112008002073

[8] Perret, L., "PIV Investigation of the Shear Layer Vortices in the Near Wake of a Circular Cylinder," *Experiments in Fluids*, Vol. 47, Nos. 4–5, 2009, pp. 789–800. doi:10.1007/s00348-009-0665-y

[9] Deck, S., and Thorigny, P., "Unsteadiness of an Axisymmetric Separating-Reattaching Flow: Numerical Investigation," *Physics of Fluids*, Vol. 19, No. 6, 2007, pp. 065103-1–065103-20. doi:10.1063/1.2734996

[10] Weiss, P.-É., Deck, S., Robinet, J.-C., and Sagaut, P., "On the Dynamics of Axisymmetric Turbulent Separating/Reattaching Flows," *Physics of Fluids*, Vol. 21, No. 7, 2009, pp. 075103-1–075103-8. doi:10.1063/1.3177352

[11] Weiss, P.-É., and Deck, S., "Control of the Antisymmetric Mode ($m = 1$) for High Reynolds Axisymmetric Turbulent Separating/Reattaching Flows," *Physics of Fluids*, Vol. 23, No. 9, 2011, pp. 095102-1–095102-19. doi:10.1063/1.3614481

[12] You, Y., Lüdeke, H., and Hannemann, V., "Detached Eddy Simulation of Base Flows Under Subsonic Free Stream Conditions," Sonderforschungsbereich/Transregio 40—Annual Report 2010, 2010, pp. 137–148, http://www.sfbtr40.de/images/stories/annualreport2010/b5%20detached.pdf [retrieved 10 April 2012].

[13] Widnall, S. E., Bliss, D. B., and Tsai, C.-Y., "The Instability of Short Waves on a Vortex Ring," *Journal of Fluid Mechanics*, Vol. 66, No. 1, 1974, pp. 35–47. doi:10.1017/S0022112074000048

[14] Darmofal, D. L., "The Role of Vorticity Dynamics in Vortex Breakdown," AIAA Paper 1993-3036, July 1993.

[15] Hannemann, K., Lüdeke, H., Pallegoix, J.-F., Ollivier, A., Lambaré, H., Maseland, J. E. J., Geurts, E. G. M., Frey, M., Deck, S., Schrijer, F. F. J., Scarano, F., and Schwane, R., "Launch Vehicle Base Buffeting—Recent Experimental and Numerical Investigations," *Proceedings of the 7th European Symposium on Aerothermodynamics for Space Vehicles*, ESA-SP692, The European Space Agency, Noordwijk, The Netherlands, 2011.

[16] Wolf, C. C., You, Y., Hörnschemeyer, R., Lüdeke, H., and Hannemann, V., "Base-Flow Sensitivity of a Generic Rocket Forebody Towards Small Freestream Angles," *4th European Conference for Aerospace Sciences (EUCASS)*, Torus Press, Moscow, Russia, July 2011.

[17] Bitter, M., Scharnowski, S., Hain, R., and Kähler, C. J., "High-Repetition-Rate PIV Investigations on a Generic Rocket Model in Sub- and Supersonic Flows," *Experiments in Fluids*, Vol. 50, 2010, pp. 1019–1030. doi:10.1007/s00348-010-0988-8

[18] Saile, D., Gülhan, A., and Henckels, A., "Investigations on the Near-Wake Region of a Generic Space Launcher Geometry," AIAA Paper 2011-2352, April 2011.

[19] Ganapathisubramani, B., Lakshminarasimhan, K., and Clemens, N. T., "Determination of Complete Velocity Gradient Tensor by Using Cinematographic Stereoscopic PIV in a Turbulent Jet," *Experiments in Fluids*, Vol. 42, No. 6, 2007, pp. 923–939. doi:10.1007/s00348-007-0303-5

[20] Haigermoser, C., Scarano, F., and Onorato, M., "Investigation of the Flow in a Circular Cavitiy Using Stereo and Tomographic Particle Image Velocimetry," *Experiments in Fluids*, Vol. 46, No. 3, 2008, pp. 517–526. doi:10.1007/s00348-008-0577-2

[21] Schäfer, L., Dierksheide, U., Klaas, M., and Schröder, W., "Investigation of Dissipation Elements in a Fully Developed Turbulent Channel Flow by Tomographic Particle-Image Velocimetry," *Physics of Fluids*, Vol. 23, No. 3, 2011, pp. 035106-1–035106-11. doi:10.1063/1.3556742

[22] Elsinga, G. E., Scarano, F., Wieneke, B., and van Oudheusden, B. W., "Tomographic Particle Image Velocimetry," *Experiments in Fluids*, Vol. 41, No. 6, 2006, pp. 933–947. doi:10.1007/s00348-006-0212-z

[23] Herman, G. T., and Lent, A., "Iterative Reconstruction Algorithms," *Computers in Biology and Medicine*, Vol. 6, No. 4, 1976, pp. 273–294. doi:10.1016/0010-4825(76)90066-4

[24] Wieneke, B., "Volume Self-Calibration for 3D Particle Image Velocimetry," *Experiments in Fluids*, Vol. 45, No. 4, 2008, pp. 549–556. doi:10.1007/s00348-008-0521-5

[25] Haller, G., "An Objective Definition of a Vortex," *Journal of Fluid Mechanics*, Vol. 525, Feb. 2005, pp. 1–26. doi:10.1017/S0022112004002526

[26] Hunt, J. C. R., Wray, A. A., and Moin, P., "Eddies, Streams, and Convergence Zones in Turbulent Flows," Proceedings of the Summer Program 1988, NASA CTR-S88, Dec. 1988, pp. 193–208.

[27] Zhou, J., Adrian, R. J., Balachandar, S., and Kendall, T. M., "Mechanisms for Generating Coherent Packets of Hairpin Vortices in Channel Flow," *Journal of Fluid Mechanics*, Vol. 387, May 1999, pp. 353–396. doi:10.1017/S002211209900467X

[28] Chakraborty, P., Balachandar, S., and Adrian, R. J., "On the Relationships Between Local Vortex Iidentification Schemes," *Journal of Fluid Mechanics*, Vol. 535, July 2005, pp. 189–214. doi:10.1017/S0022112005004726

D. Papamoschou
Associate Editor